

Electronic structure of InP/ZnSe quantum dots: effect of tetrahedral shape, valence band coupling and excitonic interactions

Josep Planelles and Juan I. Climente

Dept. de Química Física i Analítica, Universitat Jaume I, 12080, Castelló, Spain

(Dated: December 11, 2025)

The energy levels and optical transitions of tetrahedral core/shell InP/ZnSe quantum dots (QDs) are investigated by means of multi-band k-p theory. Despite the \bar{T}_d symmetry relaxing spherical selection rules, the near-band-edge excitonic spectrum is reminiscent of that obtained for spherical nanocrystals. Exceptions appear in large (red-emitting) QDs, where transitions violating the (quasi-)angular momentum selection rule ($\Delta L = 0, \pm 2$) are observed, and the ground state does not become dark ($P_{3/2}$ -like). Valence band coupling is important in determining the symmetry, degeneracy and energy of hole states, with split-off holes playing a greater role than in CdSe QDs. The ($1S_e$ -like) electron ground state exhibits moderate delocalization into the ZnSe shell. The confinement regime is then strong even for thick shells, which results in Coulomb interactions being mostly perturbative. Electrons remain largely localized in the InP core even in negative trions, despite electron-electron repulsions. At the same time, the asymmetry between Coulomb attractions and repulsions leads to negative (positive) trions being bound (antibound) by tens of meV. The biexciton binding energy switches from positive to negative, depending on the QD size.

I. INTRODUCTION

InP/ZnSe nanocrystals offer a compelling alternative to traditional cadmium-based QDs due to their lower toxicity and comparable optoelectronic properties.[1, 2] The core/shell architecture of InP/ZnSe QDs, where an InP core is encapsulated by a ZnSe shell, effectively passivates surface defects and enhances photoluminescence quantum yield, making them highly suitable for applications in light-emitting diodes, bioimaging and photovoltaics.[1–7] The synthesis of these QDs typically involves colloidal methods, which allow for precise control over the core and shell sizes, as well as on their interface, thereby enabling tunable emission with relatively narrow linewidths across the visible spectrum.[8–13]

Reliable modeling of the electronic structure of InP/ZnSe QDs is a pre-requisite to rationalize and guide further experimental progress. To date, efforts in this direction have included effective mass (single-band, k-p)[9, 10, 14] and density functional theory[15] studies of hetero-nanocrystals. These works underline the parallelism between InP/ZnSe QDs and the well-known system of CdSe/CdS QDs. That is, holes are largely localized inside the InP core, while electrons – having a much lower effective mass – show some penetration into the ZnSe shell. As a result, the ZnSe shell not only prevents traps on the InP core[5, 16], but it also provides a means of modulating the excitonic energy and oscillator strength. Experiments are however contradictory at this regard. On the one hand, exciton emission is sensitive to the first monolayers of ZnSe shell only[9, 11]. On the other hand, trion and biexciton Auger rates show substantial sensitivity to the shell thickness[4, 12, 17, 18]. The question arises whether electron-electron repulsions induce a transition from type-I to quasi-type-II behavior.[17]

Recently, we have employed a multi-band k-p Hamiltonian to describe the energy levels of (non-interacting)

electrons and holes in InP/ZnSe QDs.[19] By comparing with one and two-photon absorption spectra, as well as with transient absorption measurements, it was established that the band offset between the core and shell materials departs from natural band offsets calculated from first principles for InP/ZnSe semi-bulk interfaces.[20] Specifically, the valence band offset is deeper (at least 0.69 eV), and the conduction band offset is shallower (at most 0.71 eV). This deviation may arise from dipoles at the InP-ZnSe interface, and/or from lattice-mismatch strain.[14] With such band offsets, a spectral assignment was proposed. The assignment was conducted assuming spherical shape, and hence the same symmetry labeling as for CdSe QDs.[21, 22]

Several questions remain however to be answered. (i) InP and InP/ZnSe QDs tend to present tetrahedral shape.[1, 8, 23] What is the impact on the energies, degeneracies and optical selection rules, as compared to the spherical approximation? (ii) How relevant is the valence band mixing for typical QD sizes, and near band edge emission? This aspect has been overlooked in earlier simulations,[9, 10, 14] but it was critical to understand excitonic features of Cd chalcogenide QDs.[21, 22, 24, 25] (iii) Is the spectral assignment of Ref. 19 still valid when excitonic interactions are considered? (iv) Do carrier-carrier interactions induce a transition from type-I system (for excitons) towards a quasi-type-II system (for negative trions and biexcitons)?

In this work, we answer the questions above. To that end, we compare the energy structure and optical spectrum of spherical and tetrahedral InP/ZnSe QDs, using a multi-band k-p Hamiltonian and configuration interaction (CI) method to account for carrier-carrier interactions.

We find that, despite the different envelope symmetry and the strong confinement, the optoelectronic properties of tetrahedral InP/ZnSe QDs are reminiscent of those of zinc-blende QDs with spherical shape, both at

single- and multi-particle level. Qualitative differences arise mainly for large (dark-red emitting) QDs, and include the appearance of otherwise forbidden transitions, as well as the absence of a dark ($P_{3/2}$) ground state in the valence band. Valence band mixing plays an important role in determining the hole ground state energy and degeneracy, which deviates from single-band model expectations. The inclusion of Coulomb interactions produces a fairly rigid redshift of the exciton absorption spectra, with scarce influence on the energy splitting between low-energy peaks. This reinforces the spectral assignment we proposed in Ref. 19. At the same time, repulsions give rise to large antibinding energies for positive trions and biexcitons, and to moderate binding energies for negative trions. Changes in the electronic density are however minor, as the quantum confinement exerted by the core remains as the main physical force.

II. THEORETICAL MODEL

A. Single particle states

Non-interacting electron and hole states in zinc-blende heterostructures are calculated using two-band (Γ_6) and six-band (coupled Γ_8 and Γ_7 bands) k-p Hamiltonians. Thus, we aim at obtaining spinorial wave functions of the form:

$$|n_e\rangle = \sum_{i=1}^2 f_{n_e,i}(\mathbf{r}_e) |u_i\rangle, \quad (1)$$

$$|n_h\rangle = \sum_{i=3}^8 f_{n_h,i}(\mathbf{r}_h) |u_i\rangle. \quad (2)$$

Here, $f_{n_e,i}(\mathbf{r})$ are the electron envelope functions, and $f_{n_h,i}(\mathbf{r})$ those of the hole. $|u_i\rangle$ stands for the Bloch functions, defined as in Ref.[26]. For electrons, they have Γ_6 symmetry and Bloch angular momentum $j = 1/2$:

$$\begin{aligned} |u_1\rangle &= |\Gamma_6, 1/2, +1/2\rangle = S \uparrow, \\ |u_2\rangle &= |\Gamma_6, 1/2, -1/2\rangle = S \downarrow. \end{aligned} \quad (3)$$

For heavy holes (HH) and light holes (LH), they have Γ_8 symmetry and Bloch angular momentum $j = 3/2$:

$$\begin{aligned} |u_3\rangle &= |\Gamma_8, 3/2, +3/2\rangle = (1/\sqrt{2})(X + iY) \uparrow, \\ |u_4\rangle &= |\Gamma_8, 3/2, +1/2\rangle = (1/\sqrt{6})[(X + iY) \downarrow - 2Z \uparrow], \\ |u_5\rangle &= |\Gamma_8, 3/2, -1/2\rangle = -(1/\sqrt{6})[(X - iY) \uparrow + 2Z \downarrow], \\ |u_6\rangle &= |\Gamma_8, 3/2, -3/2\rangle = -(1/\sqrt{2})(X - iY) \downarrow. \end{aligned} \quad (4)$$

For split-off holes (SOH), they have Γ_7 symmetry and Bloch angular momentum $j = 1/2$:

$$\begin{aligned} |u_7\rangle &= |\Gamma_7, 1/2, +1/2\rangle = (1/\sqrt{3})[(X + iY) \downarrow + Z \uparrow], \\ |u_8\rangle &= |\Gamma_7, 1/2, -1/2\rangle = (1/\sqrt{3})[(X - iY) \uparrow - Z \downarrow]. \end{aligned} \quad (5)$$

The corresponding hamiltonian for electrons (two-band but diagonal) is:

$$H_e = \frac{\hbar^2}{2m_0} \left(\mathbf{p} \frac{1}{m_e(\mathbf{r})} \mathbf{p} \right) + V_e(\mathbf{r}), \quad (6)$$

with m_0 the free-electron mass, \mathbf{p} the momentum operator, $m_e(\mathbf{r})$ the position-dependent effective mass of the electron and $V_e(\mathbf{r})$ the potential felt by the electron:

$$V_e(\mathbf{r}) = \begin{cases} E_g^{\text{InP}} & \text{if } \mathbf{r} \in \text{InP}, \\ E_g^{\text{InP}} + cbo & \text{if } \mathbf{r} \in \text{ZnSe}, \end{cases} \quad (7)$$

where E_g^{InP} is the bulk band gap of InP, and cbo the InP/ZnSe conduction band offset.

The hole Hamiltonian, projected onto $\{|u_3\rangle, \dots, |u_8\rangle\}$, with z along the $[001]$ crystallographic direction, reads:[26]

$$H_h = \begin{pmatrix} U+V & -S & R & 0 & \frac{1}{\sqrt{2}}S & -\sqrt{2}R \\ -S^\dagger & U-V & 0 & R & \sqrt{2}V & -\sqrt{\frac{3}{2}}S \\ R^\dagger & 0 & U-V & S & -\sqrt{\frac{3}{2}}S^\dagger & -\sqrt{2}V \\ 0 & R^\dagger & S^\dagger & U+V & \sqrt{2}R^\dagger & \frac{1}{\sqrt{2}}S^\dagger \\ \frac{1}{\sqrt{2}}S^\dagger & \sqrt{2}V & -\sqrt{\frac{3}{2}}S & \sqrt{2}R & U-\Delta & 0 \\ -\sqrt{2}R^\dagger & -\sqrt{\frac{3}{2}}S^\dagger & -\sqrt{2}V & \frac{1}{\sqrt{2}}S & 0 & U-\Delta \end{pmatrix}. \quad (8)$$

Here, Δ is the spin-orbit energy separating SOH from HH and LH subbands. The other terms are:

$$U = -\frac{\hbar^2}{2m_0} \gamma_1 p^2 + V_h(\mathbf{r}), \quad (9)$$

$$V = -\frac{\hbar^2}{2m_0} \gamma_2 (p_\parallel^2 - 2p_z^2), \quad (10)$$

$$R = -\frac{\hbar^2}{2m_0} \sqrt{3} (\mu p_+^2 - \bar{\gamma} p_-^2), \quad (11)$$

$$S = -\frac{\hbar^2}{m_0} \sqrt{3} \gamma_3 p_- p_z, \quad (12)$$

with $\gamma_1, \gamma_2, \gamma_3$ the Luttinger parameters, $\mu = (\gamma_3 - \gamma_2)/2$ and $\bar{\gamma} = (\gamma_3 + \gamma_2)/2$. $p^2 = p_x^2 + p_y^2 + p_z^2$, $p_\parallel = p_x^2 + p_y^2$ are the components of the squared momentum and $V_h(\mathbf{r})$ the hole confining potential:

$$V_h(\mathbf{r}) = \begin{cases} 0 & \text{if } \mathbf{r} \in \text{InP}, \\ vbo & \text{if } \mathbf{r} \in \text{ZnSe}, \end{cases} \quad (13)$$

where vbo is the bulk valence band offset between InP and ZnSe. Because vbo is quite deep, holes are expected to be largely confined inside the InP core. For this reason, we have simplified H_h by considering homogeneous (InP) Luttinger parameters, rather than position-dependent ones. Lattice-mismatch strain and self-energy terms are not accounted for explicitly. Their main impact is to lower cbo . [14, 25] Because we infer this parameter from comparison with experiments, [19] the effect is implicit.

Hamiltonians H_e and H_h are integrated numerically, using the finite elements method with Comsol Multiphysics.

B. Many-body states

The Hamiltonian for excitons (X), biexcitons (XX), positive trions (X^+) and negative trions (X^-) can be written in the second quantization as:

$$\begin{aligned} \hat{H} = & \sum_i E_i^e e_i^\dagger e_i + \sum_i E_i^h h_i^\dagger h_i \\ & + \sum_{ijkl} \langle ij|kl \rangle W_{eh} |k\rangle |l\rangle e_i^\dagger h_j^\dagger h_k e_l \\ & + \frac{1}{2} \sum_{ijkl} \langle ij|kl \rangle W_{ee} |kl\rangle e_i^\dagger e_j^\dagger e_k e_l \\ & + \frac{1}{2} \sum_{ijkl} \langle ij|kl \rangle W_{hh} |kl\rangle h_i^\dagger h_j^\dagger h_k h_l, \quad (14) \end{aligned}$$

where E_i^e (E_i^h) is the electron (hole) energy in the single-particle state $|i\rangle$, e_i (h_i) is the electron (hole) annihilation operator and $\langle ij|W|kl\rangle$ is the two-body Coulomb matrix element. Electron-hole exchange terms are neglected. Coulomb matrix elements are calculated by integrating Poisson equation in a heterogeneous dielectric environment. Specifically, we consider a different dielectric constant in the inorganic QD (ε_{in}) and the surrounding –usually organic– medium (ε_{out}). Because $\varepsilon_{out} \ll \varepsilon_{in}$, this dielectric mismatch greatly enhances Coulomb interactions.[25, 27] Hamiltonian (14) is solved using a CI method.[28]

C. Optical transitions and selection rules

The probability of a transition from an initial state $|i\rangle$ to a final state $|f\rangle$ is calculated using Fermi's golden rule:

$$P_{i \rightarrow f}(h\nu) \propto \sum_\alpha |\langle f | \epsilon_\alpha p_\alpha | i \rangle|^2 \delta(E_{if} - h\nu) n_i(T) (1 - n_f(T)). \quad (15)$$

Here, α runs over the different (orthogonal) components of the polarization vector ϵ . n_j is the thermal population of the state $|j\rangle$ at temperature T , and $E_{if} = E_f - E_i$ is the energy difference between states $|i\rangle$ and $|f\rangle$. In the simulations, the resonance condition, $\delta(E_{if} - h\nu)$, is replaced by a Gaussian function of bandwidth 1 meV. The interband absorption spectrum is obtained computing $P_{i \rightarrow f}$ for all the possible transitions between near-band-edge initial excitonic states with N_e electrons and N_h holes, and final states with $N_e - 1$ electrons and $N_h - 1$ holes.

Selection rules arise from the dipole matrix element, $\langle f | \mathbf{p} | i \rangle$. In InP/ZnSe QDs, both the microscopic lattice[4] and the InP core shape[1, 8, 16, 23] have tetrahedral symmetry. Thus, the relevant point group is the double group of the tetrahedron, \bar{T}_d . Transitions are dipole-allowed if the integrand in $\langle f | \mathbf{p} | i \rangle$ belongs to the totally symmetric irreducible representation, Γ_1 .

Often, more specific selection rules can be derived by integrating envelope and Bloch parts separately. For example, an interband transition in the independent particle scheme is given by the coupling between a valence band hole state $|n_h\rangle$ and a conduction band electron state $|n_e\rangle$: [29]

$$\langle n_e | p_\alpha | n_h \rangle = \sum_{j=1}^2 \sum_{i=3}^8 \langle f_{n_e,j} | f_{n_h,i} \rangle \langle u_j | p_\alpha | u_i \rangle. \quad (16)$$

The Bloch integral, $\langle u_j | p_\alpha | u_i \rangle$, accounts for the selection rules arising from the lattice symmetry. They can be derived from Eqs. (3)-(5). In the \bar{T}_d group, the momentum operator has Γ_5 symmetry. Because the products $\Gamma_6 \times \Gamma_5 \times \Gamma_8$ and $\Gamma_6 \times \Gamma_5 \times \Gamma_7$ contain the totally symmetric representation (see Table III in Appendix A), transitions to the conduction band are allowed from HH, LH and SOH bulk bands alike.

The envelope integral, $\langle f_{n_e,j} | f_{n_h,i} \rangle$ provides an additional restriction, related to the QD confinement. Namely, both electron and hole envelope functions must have the same symmetry. When cubic band warping is neglected, $\mu = 0$ in Eq. (11), and the confining potential is spherical, H_e and H_h present spherical symmetry. Electron states can then be labeled as $n_e L_e$, where L_e is the envelope angular momentum. The lowest states are typically $1S_e$, $1P_e$, $2S_e$, etc. Hole states, under the influence of band mixing, have well defined total angular momentum $J_h = L_h + j_h$, with L_h the angular momentum and j_h the Bloch one. The states can be labeled as $n_h (L_h)_{J_h}$, where L_h is the lowest angular momentum of the spinor. Top-most states include $1S_{3/2}$, $1P_{3/2}$, $1S_{1/2}$ and $1P_{1/2}$. [22] Within these states, valence band mixing couples envelope components differing in $\Delta L_h = 0, \pm 2$. [30] It follows that $\langle f_{n_e,j} | f_{n_h,i} \rangle \propto \delta_{L_e, L_h}$, and allowed transitions include $n_h L_{J_h} \rightarrow n_e L$ and $n_h L_{J_h} \rightarrow n_e (L + 2)$. For example, $1S_{3/2}$ has a HH component with $L_h = 0$ and a LH one with $L_h = 2$. Then, $1S_{3/2} 1S_e$ and $1S_{3/2} 1D_e$ are both allowed. These strict selection rules have provided a successful assign-

TABLE I. Envelope, Bloch and total irreducible representations of the lowest conduction (Γ_6), HH-LH (Γ_8) and SOH (Γ_7) states in \bar{T}_d . The envelope angular momentum L in the spherical limit is also given.

L	Envelope	Bloch	Total
0	Γ_1	Γ_6	Γ_6
1	Γ_5	Γ_6	$\Gamma_7 \oplus \Gamma_8$
2	$\Gamma_3 \oplus \Gamma_5$	Γ_6	$\Gamma_7 \oplus 2\Gamma_8$
0	Γ_1	Γ_8	Γ_8
1	Γ_5	Γ_8	$\Gamma_6 \oplus \Gamma_7 \oplus 2\Gamma_8$
2	$\Gamma_3 \oplus \Gamma_5$	Γ_8	$2\Gamma_6 \oplus 2\Gamma_7 \oplus 3\Gamma_8$
0	Γ_1	Γ_7	Γ_7
1	Γ_5	Γ_7	$\Gamma_6 \oplus \Gamma_8$
2	$\Gamma_3 \oplus \Gamma_5$	Γ_7	$\Gamma_6 \oplus 2\Gamma_8$

ment of the absorption spectra of CdSe QDs,[21, 24] and were recently used for InP/ZnSe QDs[19].

In InP QDs, however, the confining potential is tetrahedral and band warping may be non-negligible. Because the point group is now finite, the selection rule associated with $\langle f_{n_e,j} | f_{n_h,i} \rangle$ is relaxed. As shown in Table I, former $L = 0$, $L = 1$ and $L = 2$ orbitals acquire Γ_1 , Γ_5 and $\Gamma_3 \oplus \Gamma_5$ symmetry, respectively. Consequently, transitions between $1S_{3/2}$ and $1P_e$ states, forbidden in a spherical system, become active under a cubic perturbation, as both involve the Γ_5 representation. In addition, J is no longer a valid quantum number, which lifts the $\Delta L_h = 0, \pm 2$ restriction within the envelope components of $|n_h\rangle$.

The only general selection rule remaining is that associated with the total symmetry of $\langle n_e | p_\alpha | n_h \rangle$. Table I shows that $|n_e\rangle$ and $|n_h\rangle$ states can have total symmetries Γ_6 , Γ_7 and Γ_8 . Because the momentum operator has Γ_5 symmetry, the products $\Gamma_f \times \Gamma_5 \times \Gamma_i$ contain Γ_1 in all instances except when $\Gamma_f = \Gamma_i = \Gamma_6, \Gamma_7$. Thus, transitions to $1S_e$ -like states (total symmetry Γ_6) are possible from any HH, LH and SOH state except those with Γ_6 symmetry. Transitions to $1P_e$ -like states (total symmetry Γ_7) are possible from any hole state, except those with Γ_7 symmetry. Transitions to $1D_e$ -like states (total symmetry Γ_8) are possible from any hole state, with no restriction.

III. RESULTS

We study the electronic structure of electrons, holes, excitons, trions and biexcitons in InP/ZnSe QDs. To model the InP core, we take $m_e = 0.08$, $\gamma_1 = 5.08$, $\gamma_2 = 1.60$, $\gamma_3 = 2.1$, $\Delta = 0.108$ eV and $E_g^{\text{InP}} = 1.42$ eV.[31] In the ZnSe shell, we take $m_e = 0.16$ and $E_g^{\text{ZnSe}} = 2.82$ eV,[32, 33] but keep InP parameters for the valence band ($\gamma_1, \gamma_2, \gamma_3, \Delta$). This is a reasonable approximation because holes stay largely confined in the core, and simplifies H_h by avoiding the need of Burt-Foreman boundary conditions.[34, 35] The band offsets for the InP/ZnSe interface are $vbo = 0.9$ eV and $cbo = 0.5$ eV, which fall within the range proposed in Ref. 19. Relative dielectric constants are $\epsilon_{in} = 10$ for the QD and $\epsilon_{out} = 2$ for the organic environment. In all systems, we calculate the 10 lowest electron (30 highest hole) spinorial, non-interacting states. For excitonic systems, CI simulations use a basis built from all Hartree products of single-particle wave functions (excitons), single-particle wave functions combined with Slater determinants (trions), and products of Slater determinants (biexcitons), all derived from the non-interacting states.[28]

A. Non-interacting electron and hole

We start by comparing the (near-band-edge) energy levels of non-interacting carriers in spherical (Fig. 1a)

and tetrahedral (Fig. 1b) QDs. The shell size (r_s) is fixed and the core size (r_c) is varied. In tetrahedral QDs, r_c and r_s are distances from the center to a vertex. We consider dimensions such that electron-hole energies lie in the cyan blue-to-red spectral window. This implies larger r_c values for tetrahedra than for spheres, as their shape makes them more sensitive to confinement.

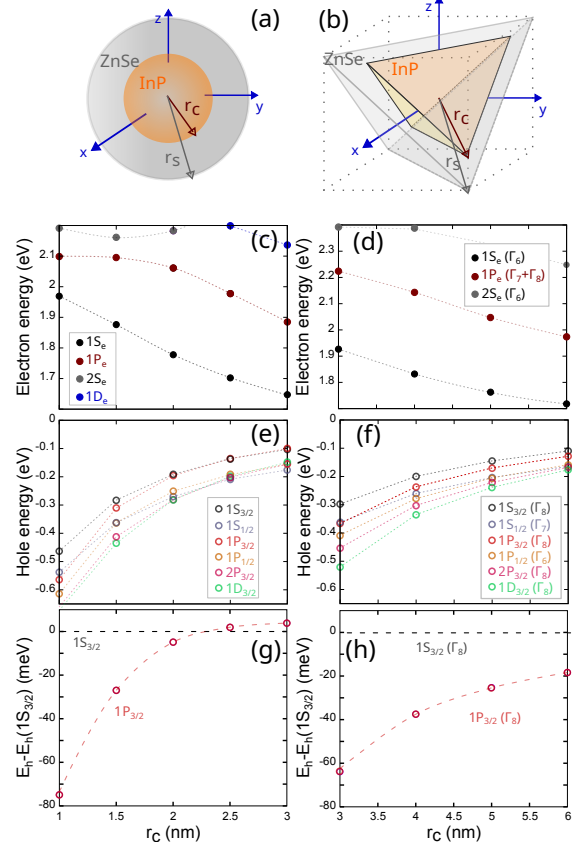


FIG. 1. Electronic structure of non-interacting electron and hole. (a) and (b): schematic of the spherical and tetrahedral core/shell QDs under study. (c) and (d): electron energy levels for varying r_c . (e) and (f): hole energy levels for varying r_c . (g) and (h): energy difference between $1P_{3/2}$ and $1S_{3/2}$ states. In spherical QDs, $r_s = 5$ nm. In tetrahedral QDs, $r_s = 8$ nm.

Figs. 1c and 1d show that electron levels display stabilization when confinement decreases, but it deviates from a simple $1/r_c^2$ trend. Also, the splitting between energy levels does not decrease with increasing r_c . These are signatures of the ZnSe shell playing a role. We come back to this point below. At this stage, we wish to underline the parallelism between states in spherical and tetrahedral QDs. In spherical QDs, the lowest states are easily identified as $1S_e$, $1P_e$ and $2S_e$, with degeneracies of 2, 6 and 2 – including spins. In tetrahedral QDs, the symmetries can be retrieved from the wave functions following the procedure described in Appendix B. The lowest state has Γ_6 symmetry (2-fold degenerate, see the dimension of the irreducible representations in the character table

of \bar{T}_d , Table II in Appendix A), then two states of nearly identical energy with Γ_7 (2-fold degenerate) and Γ_8 (4-fold degenerate) symmetries, and next another Γ_6 state. It is clear that a correspondence with the $1S_e$, $1P_e$ and $2S_e$ states holds despite the symmetry reduction.

Figs. 1c and 1d compare the hole states in both systems. In spherical QDs, the top-most states are $1S_{3/2}$, $1P_{3/2}$ and $1S_{1/2}$, which present the same degeneracies as their tetrahedral counterparts, with Γ_8 , Γ_8 and Γ_7 symmetries. That is, a clear correspondence is found again between the spherical states and their tetrahedral counterparts. For this reason, in what follows we label the states of both systems using the usual spherical notation, nL_J .

A few qualitative aspects differ between spherical and tetrahedral QDs, however. For example, in spherical QDs, the hole ground state switches from $1S_{3/2}$ (bright) to $1P_{3/2}$ (dark) when $r_c > 2$ nm. This is better seen in Fig. 1g, which represents the energy difference with respect to $1S_{3/2}$. The switch vanishes in tetrahedral QDs, Fig. 1h. The reason is that $1S_{3/2}$ and $1P_{3/2}$ share Γ_8 symmetry, so that an anticrossing (rather than a crossing) takes place. This result anticipates that a gradual change in the ground state properties of InP/ZnSe QDs should be expected for large enough sizes. A similar effect was reported in tetrahedral CdS QDs, albeit the crossover there occurred for decreasing (rather than increasing) radii.[25]

Insight into the role of the ZnSe shell is given in Figure 2. Figs. 2a and 2b show charge densities of electron and hole states in a spherical QD with $r_c=1.5$ nm (orange-to-red emission). Holes are largely confined within the InP core, because vbo is high and hole masses are heavy. By contrast, electron states penetrate into the ZnSe shell. The effect is already visible for $1S_e$, but it becomes much more pronounced for $1P_e$ and $2S_e$, as their energy largely exceeds cbo . The same behavior is observed in tetrahedral QDs, Figs. 2c and 2d, albeit the penetration of $1S_e$ is comparatively smaller. The fact that $1S_e$ is largely localized in the core, while $1P_e$ and $2S_e$ are not, is responsible for the large energy splitting between ground and excited states in Fig. 1c. With increasing r_c , $1S_e$ is stabilized but $1P_e$ and $2S_e$ less so. We shall see below the energetic isolation of $1S_e$ makes Coulomb interactions perturbative.

The significance of valence band mixing can be studied by analyzing the composition of hole states. We find that, as in spherical CdSe QDs,[22] HH and LH are strongly mixed, with equal contribution to the composition of all the states. Unlike in CdSe, however, SOH now has a significant influence. As indicated in Fig. 2b and 2d, the $1S_{3/2}$ ground state has sizable SOH character (8% in the tetrahedral QD). Excited hole states present increasing SOH character, with some states like $1S_{1/2}$ being of dominant SOH origin. The complex valence band structure will be relevant in the spectral assignment, as we show next.

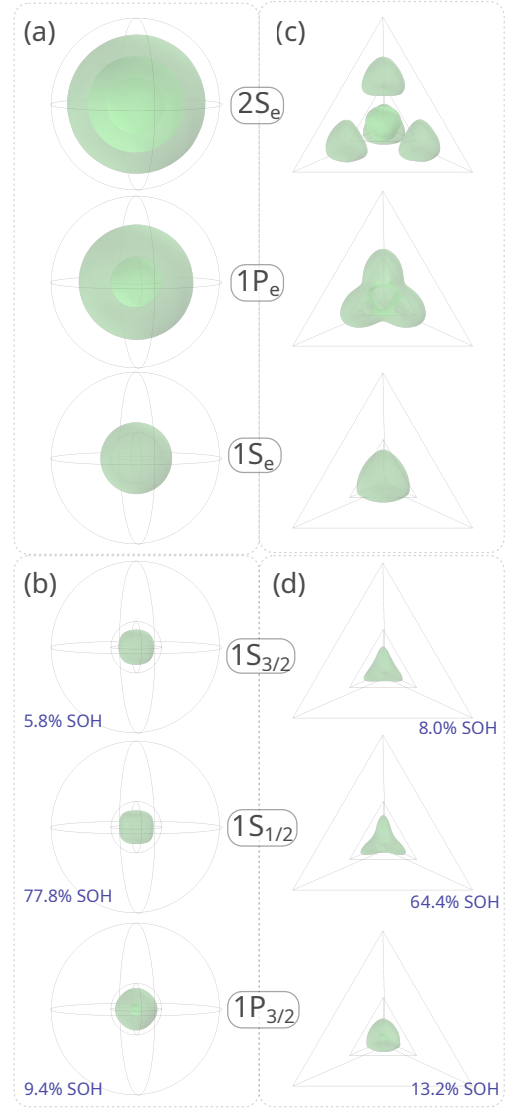


FIG. 2. Charge density of near band edge electrons (a) and holes (b) in a spherical QD with $(r_c, r_s) = (1.5, 5)$ nm. (c) and (d): same but for a tetrahedral QD with $(r_c, r_s) = (3.0, 8.0)$ nm. The isosurfaces contain 70% of the charge density.

B. Excitonic spectrum

In Figure 3, we represent the absorption spectrum of InP/ZnSe QDs, for the same geometries studied in Fig. 2. The top curve in Fig. 3a shows the absorption of a non-interacting electron-hole pair ($e-h$) in a spherical QD, while the bottom curve shows that including excitonic interactions (X). Clearly, the effect of Coulomb interactions on the main transitions of the spectrum ($1S_{3/2}1S_e$, $1S_{1/2}1S_e$, $2S_{3/2}1S_e$, $1S_{3/2}2S_e$) is but a fairly rigid red-shift of ~ 0.2 eV. In other words, excitonic interactions are strong –stimulated by dielectric confinement– but act chiefly as a first-order perturbation. This is because, as mentioned before, $1S_e$ is energetically far from the excited electron states (see Fig. 1c). Then, the electron-

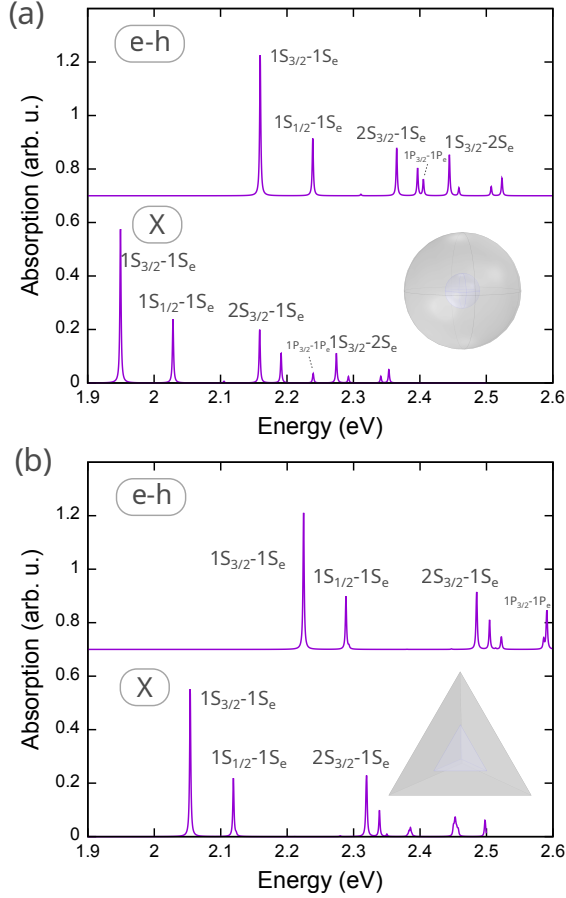


FIG. 3. Spectral assignment of the lowest transitions in the absorption of InP/ZnSe QDs. (a) Spherical QD with $(r_c, r_s) = (1.5, 5.0)$ nm. (b) Tetrahedral QD with $(r_c, r_s) = (3.0, 8.0)$ nm. In each panel, the top spectrum gives the absorption of non-interacting electron-hole pairs, and the bottom one that of interacting excitons. The insets represent the geometry under study. In the calculation, $T = 0$ K.

hole attraction does not suffice to correlate $1S_e$ and $1P_e$ states.

When the tetrahedral shape of the QD is taken into account, Fig. 3b, the main transitions of the absorption spectrum remain the same: $1S_{3/2}1S_e$, $1S_{1/2}1S_e$ and $2S_{3/2}1S_e$. We then conclude that the spectral assignment drafted in Ref. 19 is qualitatively valid in the presence of excitonic interactions and tetrahedral confinement.

A systematic comparison of the core size dependence in spherical and tetrahedral QDs is given in Fig. 4a and Fig. 4b, respectively. A few relevant observations can be drawn. (i) The band edge transition ($1S_{3/2}1S_e$, reference energy) gains oscillator strength with increasing core size. This is because $1S_e$ becomes increasingly localized in the core, maximizing its overlap with the hole ground state. (ii) The $1S_{1/2}1S_e$ transition stays 60–70 meV from the band edge transition, irrespective of the size. This is because $1S_{3/2}$ and $1S_{1/2}$ wave functions are similar – see Fig. 2–, and hence feel confinement similarly. Their

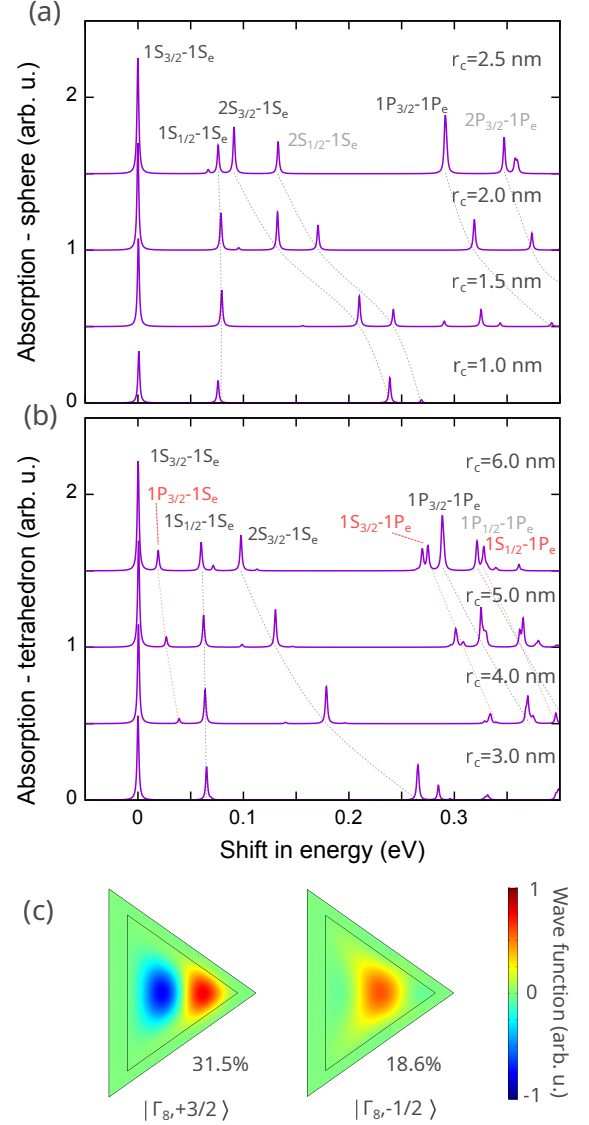


FIG. 4. Absorption spectrum of X in (a) spherical and (b) tetrahedral QDs with different core size. The spectra are off-set vertically for clarity. Dotted lines are guides to the eyes. Red lines and characters are used to highlight transitions forbidden in spherical QDs. The energy reference is that of the $1S_{3/2}1S_e$ transition. (c) Wave function of the main HH and secondary LH components of $1P_{3/2}$ when $r_c = 6$ nm. The numbers give the weight of the component within the state.

splitting is largely set by the bulk spin-orbit interaction. (iii) By contrast, the $2S_{3/2}1S_e$ transition approaches the band edge one with increasing r_c . This is because $2S_{3/2}$, with its radial node, is more sensitive to the confinement than $1S_{3/2}$. In the absorption experiments of Ref. 19, red-emitting QDs exhibited an excited transition 0.2 eV above the fundamental one, whose splitting increased to 0.33 eV in green emitting QDs. As shown in Fig. 4, both the magnitude and the size-sensitivity of the splitting reinforce the hypothesis that such a transition is $2S_{3/2}1S_e$.

(iv) Transitions involving excited electron states (such as $1P_{3/2}1P_e$) are high in energy, despite the ZnSe shell relaxing the electron confinement. These are only strong for the largest cores, as otherwise $1P_e$ delocalizes over the shell. (v) In tetrahedral QDs with large cores, a number of transitions build up, which have no correspondence in spherical QDs. These transitions are labeled with red characters in Fig. 4b. The origin of these transitions is the relaxed selection rules in the \bar{T}_d group, discussed in Section II C. As mentioned above, for large cores, $1S_{3/2}$ -like and $1P_{3/2}$ -like states anticross and mix (both have Γ_8 symmetry). Consequently, transitions such as $1P_{3/2}1S_e$ ($\Gamma_8 \rightarrow \Gamma_6$ in \bar{T}_d) become visible. The mixing of different angular momenta in tetrahedral QDs is illustrated in Fig. 4c. The left panel shows the wave function of the dominant HH component in the $1P_{3/2}$ state. As expected, a p -like orbital can be identified. The right panel, however, shows one of the LH components of the same state, where a s -like function is forming. No such component exists when the Hamiltonian is spherical, as they follow $\Delta L_h = 0 \pm 2$. [30] It is this s -like, totally symmetric (Γ_1) envelope component that enables optical coupling with the $1S_e$ -like electron. To our knowledge, no experimental evidence of these transitions has been reported to date. They likely fall within the bandwidth of more intense, spherical symmetry-allowed transitions, such as the $1S_{3/2}1S_e$ one.

The different nature of the hole ground state in large spherical or tetrahedral QDs manifests in the emission spectrum as well. In Figure 5 we plot the calculated spectra at $T = 300$ K. For spherical QDs, Fig. 5a, with increasing r_c the band edge emission first gains oscillator strength—because the $1S_e$ state becomes more localized in the core—but then decreases again (see $r_c \geq 2.5$ nm). The latter effect is because the bright $1S_{3/2}1S_e$ exciton starts sharing population with the dark $1P_{3/2}1S_e$ one. No such effect is however observed in tetrahedral QDs, Fig. 5b.

The fact that deviations between spherical and tetrahedral shape reveal for large QDs, as shown in this section and in the previous one, is somewhat surprising. One could expect them to show up in small QDs instead, when tetrahedral confinement is sensed more strongly. The underlying reason is that the cubic lattice symmetry is ultimately responsible for the T_d features. In zinc-blende QDs, cubic band warping terms are often neglected, and the spherical approximation provides a good description of the energy spectrum. In the weak confinement regime, however, the level spacing becomes small enough that band warping terms mix the states and re-establish the underlying cubic symmetry of the lattice.

C. Charged excitons and biexcitons

The effect of multi-carrier interactions is studied in Figure 6. In Fig. 6a we compare the emission of excitons, trions and biexcitons in two tetrahedral QDs with

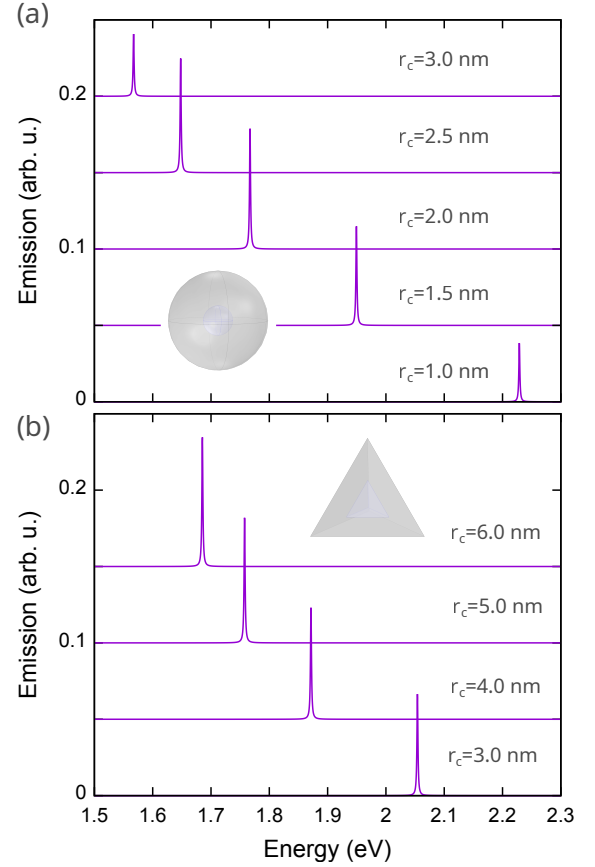


FIG. 5. Emission spectrum of X in InP/ZnSe QDs with (a) spherical and (b) tetrahedral shape, as a function of the core size. The population of states is calculated at $T = 300$ K. Shell sizes are the same as in Fig. 4.

different sizes. One can see that X^- is systematically redshifted with respect to the exciton (that is, it is bound), while X^+ is systematically blueshifted (antibound). In turn, XX can switch from antibound to bound depending on the QD dimensions. For all the excitonic species and QD sizes we investigate, electron correlations are weak. The spectroscopic shifts observed in the figure thus arise mainly from first order Coulomb perturbations. For example, in the QD with $(r_c, r_s) = (2, 6)$ nm, the non-interacting ground state has $\langle V_{ee} \rangle = 249$ meV, $\langle V_{eh} \rangle = -273$ meV and $\langle V_{hh} \rangle = 331$ meV. That is, electron repulsions are weaker because charges partially delocalize into the shell, hole repulsions are stronger because of the almost complete localization into the core, and exciton attractions are in between. Consequently, in X^- attractions prevail over attractions, which results in a redshift (binding energy). The first order perturbation estimate is $\Delta E_{X^-}^{(1)} = \langle V_{eh} + V_{ee} \rangle = -24$ meV, in close agreement with the CI calculation of Fig. 6a. On the other hand, in X^+ repulsions prevail over attractions. The perturbational estimate, $\Delta E_{X^+}^{(1)} = \langle V_{eh} + V_{hh} \rangle = 58$ meV is somewhat larger than the blueshift of $\Delta E_{X^+} = 44$ meV obtained from CI calculations, which indicates that

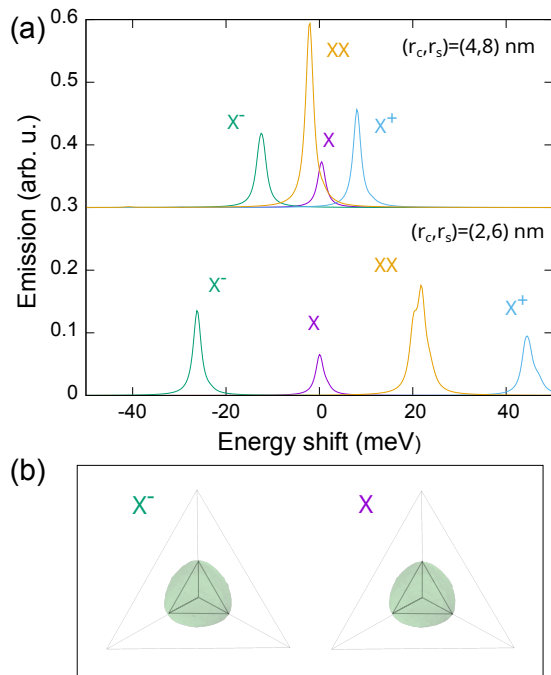


FIG. 6. (a) Emission spectrum of excitons, trions and biexcitons in two InP/ZnSe QDs with different sizes. A temperature of $T = 300$ K is assumed to calculate the population of states. The reference energy is that of X emission. (b) Charge density of a single electron within the negative trion (left) and exciton (right) ground state, for the QD with $(r_c, r_s) = (2, 6)$ nm. The isosurfaces contain 80% of the charge density.

hole-hole correlations do relax repulsions.

The weakness of electronic correlations implies that the charge density of X and X^- is similar despite electron-electron repulsions. This can be seen in Fig. 6b, where we compare isosurfaces containing 80% of the electron charge density within X^- (left) and X (right). The delocalization into the shell is nearly identical, even though we have chosen a small core ($r_c = 2$ nm) to promote tunneling. This result is at odds with the interpretation of Auger decay rates of X^- in InP/ZnSe QDs, given in Ref. 17. With increasing ZnSe shell thickness, the authors observed slower Auger rates, which was tentatively ascribed to a greater delocalization of electrons into the shell, fostered by repulsions. In view of our results, we posit the observed trend may rather be connected with the suppressed dielectric confinement (and hence weaker Coulomb interactions) in thick shell InP/ZnSe QDs.

As mentioned before, the perturbative character of Coulomb interactions involving electrons, despite the strong repulsions ($\langle V_{ee} \rangle \sim 250$ meV), is a consequence of the core/shell structure. As shown in Fig. 1d, $1S_e$ electrons are split from $1P_e$ and $2S_e$ states by $\Delta E \geq 300$ meV. That is, confinement energies exceed Coulomb ones. This is true for all the core sizes we study.

A final comment is worth on the ground state degeneracy of the excitonic species. In the tetrahedral QDs,

disregarding electron-hole exchange interaction, we obtain an 8-fold degeneracy for X , 4-fold for X^- , 10-fold for X^+ and 5-fold for XX . This result is consistent with that expected in spherical, zinc-blende QDs under the influence of valence band coupling.[36] In a non-interacting particle scheme, electrons have a total Bloch angular momentum $j = 1/2$ and holes $j = 3/2$. $1S_e$ and $1S_{3/2}$ states are then 2-fold and 4-fold degenerate, respectively, which explains the 8-fold degeneracy of X . Two interacting electrons form a singlet ground state with $J_e = 0$, which explains the 4-fold degeneracy of X^- . In turn, two interacting holes give rise to $J_h = 3/2 \times 3/2 = 3 \oplus [2] \oplus 1 \oplus [0]$. Only $J_h = 2$ and $J_h = 0$ are antisymmetric with respect to permutation, and the former is slightly stabilized by hole-hole exchange interaction. This explains the 10-fold degeneracy of X^+ and the 5-fold degeneracy of XX . The $J_h = 0$ two-hole state is only a few meV away in energy, and it is responsible for the asymmetric bandshape of XX and X^+ in Fig. 6a (bottom spectrum).

IV. CONCLUSIONS

By means of multi-band k-p Hamiltonians, combined with CI simulations and symmetry point group analysis, we have shown that:

(i) The near-band-edge electronic structure of InP/ZnSe QDs with tetrahedral shape and cubic lattice is similar to that of spherical QDs in the quasicubic ($\mu = 0$) lattice approximation, in terms of degeneracies and optical selection rules. Deviations arise for large (dark red emitting) QDs only, where $S_{3/2}$ and $P_{3/2}$ states (both with Γ_8 symmetry in the \bar{T}_d group) admix.

(ii) Valence band mixing is key to understanding the symmetry, composition and degeneracy of hole states. HH-LH coupling is as strong as in spherical, zinc-blende QDs[22], and SOH has non-negligible contributions, including the formation of low-energy $1S_{1/2}$ states.

(iii) Excitonic interactions are mostly perturbative for low-lying states, which reinforces the spectral assignment (based on a non-interacting model) of Ref. 19.

(iv) Electron-electron interactions are mostly perturbative as well. Repulsions in X^- do not lead to a significant increase of the electron delocalization into the shell. The perturbative character of the Coulomb interactions involving electrons is because the $1S_e$ state is in a strong confinement regime. Unlike excited states, its penetration into the ZnSe shell is moderate. The localization in the core stabilizes the state, leading to energy gaps with $1P_e$ and $2S_e$ states exceeding Coulomb repulsions.

ACKNOWLEDGMENTS

We acknowledge support from Grant No. PID2024-162489NB-I00, funded by Ministerio de Ciencia, Innovación y Universidades (MICIU/AEI/10.13039/501100011033/ FEDER, EU).

The data that support the findings of this article are openly available.[37]

Appendix A: Character table and products of irreducible representations in \bar{T}_d

To facilitate the discussion, we reproduce here the character table of the \bar{T}_d group[38] using Mulliken notation. The dimension of the irreducible representation gives the degeneracy of the states (e.g. 4 for Γ_8). The character under C_3 permits discriminating Γ_7 and Γ_8 states, as explained in Appendix B. The tables of products are used to determine the selection rules in Section II C.

Appendix B: Determination of the symmetry of states in \bar{T}_d

The identification of Γ_8 states is straightforward because they are four-fold degenerate (see Table II). To discriminate the Γ_6 and Γ_7 doublets, we notice that they have different characters under the C_3 : $\chi^{(\Gamma_6)}(C_3) = 1$ and $\chi^{(\Gamma_7)}(C_3) = -1$. We label the states forming the doublet F_1 and F_2 . Visual identification of the symmetry under C_3 is obscured by the degeneracy of F_1 and F_2 . The character can however be calculated as:

$$\chi(C_3) = \sum_{j=1}^2 \langle F_j | C_3 | F_j \rangle = \sum_{j=1}^2 \sum_k \lambda_k \int d^3r f_{j,k}^*(\mathbf{r}) f_{j,k}(C_3^{-1}\mathbf{r}). \quad (\text{B1})$$

In this expression, $k = 1, 2$ for electron states, while $k = 3, 8$ for hole states. λ_k is the eigenvalue of C_3 when acting on the Bloch function $|u_k\rangle$. In general, $C_3 |j, m_j\rangle = e^{im_j 2\pi/3} |j, m_j\rangle$. For the Bloch functions in Eqs. (3,4,5), the following relations emerge: $\lambda_1 = e^{+i\pi/3}$, $\lambda_2 = e^{-i\pi/3}$, $\lambda_3 = -1$, $\lambda_4 = e^{+i\pi/3}$, $\lambda_5 = e^{-i\pi/3}$, $\lambda_6 = -1$, $\lambda_7 = e^{+i\pi/3}$, $\lambda_8 = e^{-i\pi/3}$.

-
- [1] G. Almeida, R. F. Ubbink, M. Stam, I. du Fossé, and A. J. Houtepen, Inp colloidal quantum dots for visible and near-infrared photonics, *Nature Reviews Materials* **8**, 742 (2023).
 - [2] H. Liu, P. Chen, Y. Cui, Y. Gao, J. Cheng, T. He, and R. Chen, Inp semiconductor nanocrystals: synthesis, optical properties, and applications, *Advanced Optical Materials* **11**, 2300425 (2023).
 - [3] Y.-H. Won, O. Cho, T. Kim, D.-Y. Chung, T. Kim, H. Chung, H. Jang, J. Lee, D. Kim, and E. Jang, Highly efficient and stable inp/znse/zns quantum dot light-emitting diodes, *Nature* **575**, 634 (2019).
 - [4] K. R. Reid, J. R. McBride, N. J. Freymeyer, L. B. Thal, and S. J. Rosenthal, Chemical structure, ensemble and single-particle spectroscopy of thick-shell inp-znse quantum dots, *Nano letters* **18**, 709 (2018).
 - [5] P. Yu, S. Cao, Y. Wang, and J. Zhao, Repercussions of the inner shell layer on the performance of cd-free quantum dots and their light-emitting diodes, *The Journal of Physical Chemistry Letters* **15**, 201 (2023).
 - [6] Y. Li, X. Hou, X. Dai, Z. Yao, L. Lv, Y. Jin, and X. Peng, Stoichiometry-controlled inp-based quantum dots: synthesis, photoluminescence, and electroluminescence, *Journal of the American Chemical Society* **141**, 6448 (2019).
 - [7] P. Yu, S. Cao, Y. Shan, Y. Bi, Y. Hu, R. Zeng, B. Zou, Y. Wang, and J. Zhao, Highly efficient green inp-based quantum dot light-emitting diodes regulated by inner alloyed shell component, *Light: Science & Applications* **11**, 162 (2022).
 - [8] M. D. Tessier, D. Dupont, K. De Nolf, J. De Roo, and Z. Hens, Economic and size-tunable synthesis of inp/zne (e= s, se) colloidal quantum dots., *Chemistry of Materials* **27**, 4893 (2015).
 - [9] R. Toufanian, A. Piryatinski, A. H. Mahler, R. Iyer, J. A. Hollingsworth, and A. M. Dennis, Bandgap engineering of indium phosphide-based core/shell heterostructures through shell composition and thickness, *Frontiers in Chemistry* **6**, 567 (2018).
 - [10] D. Hahm, J. H. Chang, B. G. Jeong, P. Park, J. Kim, S. Lee, J. Choi, W. D. Kim, S. Rhee, J. Lim, *et al.*, Design principle for bright, robust, and color-pure inp/znse x s1-x/zns heterostructures, *Chemistry of Materials* **31**, 3476 (2019).
 - [11] H. Van Avermaet, P. Schiettecatte, S. Hinz, L. Giordano, F. Ferrari, C. Nayral, F. Delpech, J. Maultzsch, H. Lange, and Z. Hens, Full-spectrum inp-based quantum dots with near-unity photoluminescence quantum efficiency, *ACS nano* **16**, 9701 (2022).
 - [12] K. Inada, D. Eguchi, and N. Tamai, Effect of the interfacial potential on elementary exciton processes in inp-based core/shell quantum dots, *The Journal of Physical Chemistry C* **128**, 10542 (2024).
 - [13] L. Giordano, P. Schiettecatte, Y. Coppel, Q. Zhao, Y. U. Staechelin, G. Bonifas, H. Van Avermaet, C. Nayral, H. Lange, A. Vantomme, *et al.*, The core/shell interface in inp/znse colloidal quantum dots, *Chemistry of Materials* **37**, 8724 (2025).
 - [14] D. Jang, Y. Han, S. Baek, and J. Kim, Theoretical comparison of the energies and wave functions of the electron and hole states between cdse-and inp-based

TABLE II. Character table of the double group \bar{T}_d .

Irrep	E	$8C_3$	$3C_2$	$6S_4$	$6\sigma_d$	\bar{E}	$8\bar{C}_3$	$3\bar{C}_2$	$6\bar{S}_4$	$6\bar{\sigma}_d$	Example of basis
Γ_1	1	1	1	1	1	1	1	1	1	1	s (spherical orbital)
Γ_2	1	1	1	-1	-1	1	1	1	-1	-1	pseudoscalar
Γ_3	2	-1	2	0	0	2	-1	2	0	0	$(2z^2 - x^2 - y^2, x^2 - y^2)$
Γ_4	3	0	-1	1	-1	3	0	-1	1	-1	Rotations (R_x, R_y, R_z)
Γ_5	3	0	-1	-1	1	3	0	-1	-1	1	$(x, y, z); (xy, yz, zx)$
Γ_6	2	1	0	$\sqrt{2}$	0	-2	-1	0	$-\sqrt{2}$	0	(u_1, u_2)
Γ_7	2	1	0	$-\sqrt{2}$	0	-2	-1	0	$\sqrt{2}$	0	(u_7, u_8)
Γ_8	4	-1	0	0	0	-4	1	0	0	0	(u_3, u_4, u_5, u_6)

TABLE III. Product of irreducible representations in the double group \bar{T}_d .

\otimes	Γ_1	Γ_2	Γ_3	Γ_4	Γ_5	Γ_6	Γ_7	Γ_8
Γ_1	Γ_1	Γ_2	Γ_3	Γ_4	Γ_5	Γ_6	Γ_7	Γ_8
Γ_2		Γ_1	Γ_3	Γ_5	Γ_4	Γ_7	Γ_6	Γ_8
Γ_3			$\Gamma_1 \oplus \Gamma_2 \oplus \Gamma_3$	$\Gamma_4 \oplus \Gamma_5$	$\Gamma_4 \oplus \Gamma_5$	Γ_8	Γ_8	$\Gamma_6 \oplus \Gamma_7 \oplus \Gamma_8$
Γ_4				$\Gamma_1 \oplus \Gamma_3 \oplus \Gamma_4 \oplus \Gamma_5$	$\Gamma_2 \oplus \Gamma_3 \oplus \Gamma_4 \oplus \Gamma_5$	$\Gamma_6 \oplus \Gamma_8$	$\Gamma_7 \oplus \Gamma_8$	$\Gamma_6 \oplus \Gamma_7 \oplus 2\Gamma_8$
Γ_5					$\Gamma_1 \oplus \Gamma_3 \oplus \Gamma_4 \oplus \Gamma_5$	$\Gamma_7 \oplus \Gamma_8$	$\Gamma_6 \oplus \Gamma_8$	$\Gamma_6 \oplus \Gamma_7 \oplus 2\Gamma_8$
Γ_6						$\Gamma_1 \oplus \Gamma_4$	$\Gamma_2 \oplus \Gamma_5$	$\Gamma_3 \oplus \Gamma_4 \oplus \Gamma_5$
Γ_7							$\Gamma_1 \oplus \Gamma_4$	$\Gamma_3 \oplus \Gamma_4 \oplus \Gamma_5$
Γ_8								$\Gamma_1 \oplus \Gamma_2 \oplus \Gamma_3 \oplus 2\Gamma_4 \oplus 2\Gamma_5$

core/shell/shell quantum dots: effect of the bandgap energy of the core material on the emission spectrum, *Optical Materials Express* **9**, 1257 (2019).

- [15] N. Du and H. Chen, Stark effects of the fluorescence spectra in inp core and inp/zns core/shell quantum dots under an external electric field, *RSC advances* **15**, 43955 (2025).
- [16] S. Kumar, C. Cocchi, and T. Steenbock, Surface defects and symmetry breaking impact on the photoluminescence of inp quantum dots, *Nano Letters* (2025).
- [17] T. Kim, Y.-H. Won, E. Jang, and D. Kim, Negative trion auger recombination in highly luminescent inp/zns/zns quantum dots, *Nano letters* **21**, 2111 (2021).
- [18] A. T. Nguyen, P. Cavanaugh, I. J.-L. Plante, C. Ippen, R. Ma, and D. F. Kelley, Auger dynamics in inp/zns/zns quantum dots having pure and doped shells, *The Journal of Physical Chemistry C* **125**, 15405 (2021).
- [19] D. Respekta, P. Schiettecatte, L. Giordano, N. De Vlamynck, P. Geiregat, J. Climente, and Z. Hens, Energy-level structure and band alignment in inp/zns core/shell quantum dots, *ACS Nano* **19**, 19831 (2025).
- [20] S.-H. Wei and A. Zunger, Calculated natural band offsets of all ii-vi and iii-v semiconductors: Chemical trends and the role of cation d orbitals, *Applied Physics Letters* **72**, 2011 (1998).
- [21] D. J. Norris and M. Bawendi, Measurement and assignment of the size-dependent optical spectrum in cdse quantum dots, *Physical Review B* **53**, 16338 (1996).
- [22] A. L. Efros and M. Rosen, Quantum size level structure of narrow-gap semiconductor nanocrystals: Effect of band coupling, *Physical Review B* **58**, 7120 (1998).
- [23] K. C. D  mbgen, J. Zito, I. Infante, and Z. Hens, Shape, electronic structure, and trap states in indium phosphide quantum dots, *Chemistry of Materials* **33**, 6885 (2021).
- [24] A. I. Ekimov, F. Hache, M. Schanne-Klein, D. Ricard, C. Flytzanis, I. Kudryavtsev, T. Yazeva, A. Rodina, and A. L. Efros, Absorption and intensity-dependent photoluminescence measurements on cdse quantum dots: assignment of the first electronic transitions, *JOSA B* **10**, 100 (1993).
- [25] V. A. Fonoberov, E. Pokatilov, and A. A. Balandin, Exciton states and optical transitions in colloidal cds quantum dots: Shape and dielectric mismatch effects, *Physical Review B* **66**, 085310 (2002).
- [26] E. Novik, A. Pfeuffer-Jeschke, T. Jungwirth, V. Latussek, C. Becker, G. Landwehr, H. Buhmann, and L. Molenkamp, Band structure of semimagnetic hg 1-y mn y te quantum wells, *Physical Review B—Condensed Matter and Materials Physics* **72**, 035321 (2005).
- [27] A. V. Rodina and A. L. Efros, Effect of dielectric confinement on optical properties of colloidal nanostructures, *Journal of Experimental and Theoretical Physics* **122**, 554 (2016).
- [28] A. Bertoni, Citool, <https://github.com/andreabertoni/citool> (2010), accessed 2025-11-27.
- [29] G. Bastard, *Wave mechanics applied to semiconductor heterostructures* (New York, NY (USA); John Wiley and Sons Inc., 1990).
- [30] A. Baldereschi and N. O. Lipari, Spherical model of shallow acceptor states in semiconductors, *Physical Review B* **8**, 2697 (1973).

- [31] I. Vurgaftman, J. Meyer, and L. R. Ram-Mohan, Band parameters for iii–v compound semiconductors and their alloys, *Journal of applied physics* **89**, 5815 (2001).
- [32] Band gap of zinc selenide (znse): Data extracted from the landolt-börnstein book series and associated databases (), accessed 2024-11-24.
- [33] Znse effective mass: Datasheet from “pauling file multinaries edition – 2022” in springermaterials (https://materials.springer.com/isp/physical-property/docs/ppp_6c3a12654a04e7a8ba8f2ce5762ef1ac) (), accessed 2024-11-24.
- [34] M. Burt, The justification for applying the effective-mass approximation to microstructures, *Journal of Physics: Condensed Matter* **4**, 6651 (1992).
- [35] B. A. Foreman, Effective-mass hamiltonian and boundary conditions for the valence bands of semiconductor microstructures, *Physical Review B* **48**, 4964 (1993).
- [36] A. Rodina and A. L. Efros, Band-edge biexciton in nanocrystals of semiconductors with a degenerate valence band, *Physical Review B* **82**, 125324 (2010).
- [37] J. Planelles and J. I. Climente, Dataset of “electronic structure of inp/znse quantum dots: effect of tetrahedral shape, valence band coupling and excitonic interactions”, doi 10.5281/zenodo.17867662 (2025).
- [38] M. S. Dresselhaus, G. Dresselhaus, and A. Jorio, *Group theory: application to the physics of condensed matter* (Springer Science & Business Media, 2007).